Multivariable DC Bias Control of a High-Power AC–DC Dual-Active-Bridge-Based Converter

José W. M. de Araújo, Dalton de A. Honório, *Member, IEEE*, and Demercil de S. Oliveira Jr., *Senior Member, IEEE*

***Abstract*—This article addresses the dc magnetization issue in high-power single-stage dual active bridge (DAB)-based converters. A multivariable control strategy capable of simultaneously regulating the dc bias currents is applied to an integrated ac–dc topology. The control approach relies on two input variables, the magnetizing current, and the secondary current dc offset, and two outputs, that is, the duty cycles applied to the primary-side and secondary-side switches. The currents are measured by Hall sensors comprising several samples to average the offset values. The locations of samples and the measurement accuracy are discussed to validate the acquisition concept. The transformer is modeled using state-space equations and the controllers are tuned using state feedback associated with an augmented system to achieve robust reference tracking and disturbance rejection. The controller is designed based on the Lyapunov equation. Experimental results are presented and discussed to validate the control strategy applied to an integrated ac–dc converter rated at 8.33 kW. Steady-state and dynamic results show that the introduced solution can eliminate the dc bias of all currents even during load changes, without significantly affecting the harmonic content of the acinput current.**

***Index Terms*—AC–DC power conversion, current control, Lyapunov methods, pulsewidth modulation (PWM), robust control.**

I. Introduction

THE dc bias is a well-known problem in isolated converters, such as push–pull, half-bridge, and full-bridge converters [1]. The main factors responsible for the dc bias in steady-state conditions are asymmetric gating signals, which, in turn, are caused by intrinsic differences among the semiconductors associated with the internal resistance, forward voltage drop, distinct turn-ON and turn-OFF times, delay, and low resolution of pulsewidth modulation (PWM) signals [2]. In low-power converters, a sufficiently high resolution of the PWM signal together with parasitic resistances of switches and windings may avoid core saturation since any dc bias can be mitigated in the parasitic resistance in a finite time. Also, the use of discrete semiconductors from the same batch or integrated modules comprising all necessary switches combined with drivers of the same manufacturer greatly contributes to reducing the production of this undesirable phenomenon in a steady state. However, this approach cannot eliminate dc bias in higher-power designs in which parasitic resistances are small [3]. Moreover, since several disturbances may occur, core saturation may lead to semiconductor failures. This is a well-known cause of sudden failures in push–pull converters [1].

In half-bridge and full-bridge converters, this phenomenon is avoided by using a series-connected capacitor or by using peak current mode controllers [4] and [5]. However, at high power levels, the high current does require the use of capacitors with low equivalent series resistances (ESRs) to reduce voltage drops and losses. Considering commercially available high-frequency capacitors nowadays, it is necessary to add several components in parallel, resulting in increased volume and cost and compromising reliability. Since the push–pull converter uses a center-tapped transformer with dc content, peak current mode control becomes a more feasible solution in this case.

In dc–dc converters with bidirectional power flow like the dual active bridge (DAB) [6], dc magnetization may be caused by both the primary and secondary bridges. Then, two series capacitors are required, one for each winding. The phase-shift (PS) angle variation can also produce a dc bias. By decreasing the transient time between two different angles is possible to reduce the dc bias produced. Modern microcontrollers can use high-resolution PWM channels combined with proper modulation techniques that can compensate for the transient effects of transformer magnetization [7]. These transient modulation improvements can be categorized in terms of distinct strategies such as single-PS (SPS) [8], dual-PS (DPS) [9], extended-PS (EPS) [10], and triple-PS (TPS) [11]. For low-power converters, any remaining dc bias will be mitigated in parasitic resistances. However, for high-power converters, this bias could cumulate and saturate the magnetic core, since its resistances are very small. This cumulative dc-bias has a slow dynamic as seen in [12] for a three-phase DAB.

Nevertheless, bidirectional single-stage ac–dc converters present a much higher complexity in terms of magnetization control [13]. The duty cycle variation along with the line voltage as required to obtain input power factor correction is a permanent source of perturbations for the magnetizing current making difficult to perform a transient modulation improvement. In addition, the use of a center-tapped transformer does not allow the use of

Manuscript received 26 January 2023; revised 20 April 2023 and 16 June 2023; accepted 25 July 2023. Date of publication 7 August 2023; date of current version 22 September 2023. This work was supported in part by the Brazilian National Council for Scientific and Technological Development (CNPq) under Grants CNPQ 313465/2021-5 and CNPQ 424035/2016-2 and in part by Equatorial Energia. Recommended for publication by Associate Editor H.S. Krishnamoorthy. *(Corresponding author: Dalton de A. Honório.)*

The authors are with the Federal University of Ceará, Fortaleza 60020-181, Brasil (e-mail: willamyma@yahoo.com.br; dalton@dee.ufc.br; demercil@dee.ufc.br).

Digital Object Identifier 10.1109/TPEL.2023.3302228

series-connected capacitors and makes the measurement of the magnetizing current magnitude somewhat difficult. On the other hand, closed-loop strategies can provide the full elimination of dc offset. The existing solutions can be classified according to the measurement method, whereas the literature does only report methods based on measuring the circulating currents or the core magnetic flux.

The current measurement may rely on the signal resulting from the subtraction of currents measured by two sensors [14], parallel inductors [15], analog adders [16], or a single sensor to measure both currents [17]. However, the accuracy and bandwidth may be compromised if the design is not carefully performed. Besides that, all these works either perform some simplification to uncouple the control loops or deal with a single bridge. Thus, a cross-coupling model and a decoupling method are presented in [18].

One can also measure the flux directly using either a second transformer [19], a Hall sensor placed in the air gap [20], or an auxiliary core, also referred to as magnetic ear [21]. Despite they provide direct flux measurements, all these methods are very complex.

As noted earlier, closed-loop approaches for regulating dc–dc converters concentrate exclusively on maintaining a constant duty cycle. However, they fail to account for how dc bias regulation affects the harmonic makeup of the current that DAB-based ac–dc converters draw. Additionally, these studies often utilize mathematical manipulations to separate primary-side and secondary-side control loops, and occasionally control is restricted to a single bridge.

This work aims to address a research gap by suggesting the implementation of a classical multivariable control technique to eliminate any residual dc bias currents that persist despite mitigating them in the parasitic resistance of a high-power DAB-based ac–dc converter with a single integrated stage. Moreover, the control methodology is intrinsically coupled, with two dc bias currents serving as inputs and the duty cycles of both bridges functioning as outputs. This solution requires no simplifications to uncouple control loops and can also be adapted to dc–dc converters.

The rest of this article is organized as follows. In Section II, the dc bias issue on DAB-based converters is examined. Section III outlines the system model and control strategy, which employs state-space equations and an augmented feedback system derived from the Lyapunov equation. A dc–dc DAB converter is employed in Section III for ease of explanation. In Section IV, the dc–dc converter topology and measurement system are briefly introduced, and the model used is also applied to the ac–dc structure. Section V provides an in-depth discussion of experimental findings that support the theoretical assumptions. Finally, Section VI presents the key takeaways of this study.

II. Observed DC Bias Problem on DAB-Based Converters

Fig. 1 shows the DAB topology. It consists of two active bridges, which can operate with different duty ratios, whereas the power transfer is controlled by adjusting the PS angle. An external inductor L_d exists in the circuit to provide an efficient power transfer.

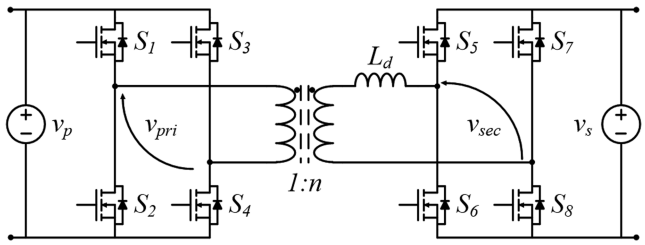

Fig. 1. DAB topology.

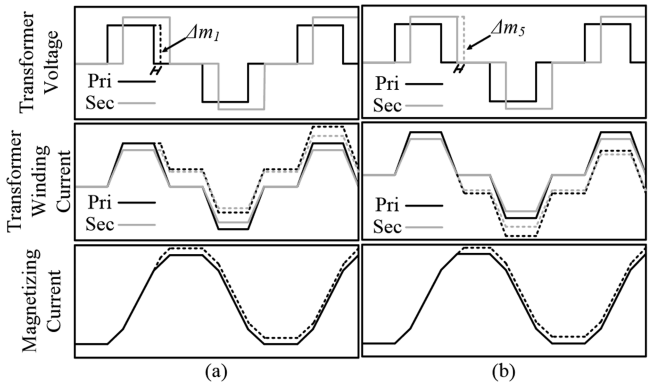

Fig. 2. Positive DC bias. (a) Primary voltage. (b) Secondary voltage.

All DAB currents are affected by the operation of both bridges. This behavior can be better understood from the analysis of Fig. 2. The solid line represents the DAB converter operating without any dc bias. A positive dc bias is added to the primary-side voltage in Fig. 2(a) by increasing Δm_1 according to the modulating signal of its respective leg, resulting in the current represented by the dashed line. One can observe that all the transformer currents corresponding to dashed lines will present a positive dc bias as a consequence.

The same positive dc bias is added to the secondary-side voltage by adding Δm_5 to the duty cycle of one leg in Fig. 2(b). Thus, the dc biases in the primary and secondary windings are negative as expected but the magnetizing current presents a positive bias instead. In this way, the addition of an incremental duty cycle produces a nonzero average value of the transformer voltage causing a dc bias in all currents.

This is a very important characteristic to be noticed for the proposed multivariable control methodology since a dc bias produced by the primary bridge must be mitigated by this very same bridge. If the secondary side bridge is considered instead, it will correctly mitigate the dc bias in the primary and secondary currents but the one associated with the magnetizing current will increase. The same behavior is valid for a dc bias produced by the secondary bridge. Thus, it is impossible to obtain a zero-dc bias in all currents actively by controlling only one bridge.

Then, it is reasonable to state that a control solution capable of eliminating the dc bias must be associated with both active bridges, as well as, either it should aggregate the capacity to

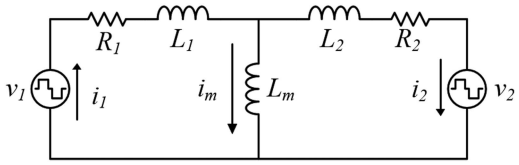

Fig. 3. Equivalent circuit of the DAB converter.

identify which bridge produced the bias or operated based on a coupled approach. Since the identification of which bridge produces the bias is not straightforward and assertive, the use of coupled methodologies becomes more feasible. Indeed, a coupled control methodology can inherently identify the bias origin, as well as the proper mitigation of the required biases by both bridges. For this purpose, it is necessary to obtain the equations involving the system currents.

III. Proposed Control Strategy

Let us consider the circuit shown in Fig. 3, in which the two bridges are replaced with a three-level voltage source, whereas the high-frequency transformer is represented by its equivalent model.

According to the work in [22], the transformer has several parasitic capacitances and inductances. Considering a conservative design, such nonidealities can be ignored for simplifying the analysis. Thus, only the primary leakage inductance L_1, the secondary leakage inductance L_2, the primary winding resistance R_1, the secondary winding resistance R_2, and the magnetizing inductance L_m are considered. L_2 and R_2 include the external power transfer inductor connected to the secondary side. The proposed analysis can be performed by referring the resistances, inductances, and voltages to the primary or secondary side considering the proper transformer turns ratio. In this way, the calculations consider only generic indices instead.

Applying Kirchhoff's current and voltage laws and considering the instantaneous average model, one can obtain

$$\begin{pmatrix} \frac{di_m}{dt} \\ \frac{di_2}{dt} \end{pmatrix} = \boldsymbol{A} \begin{pmatrix} i_m \\ i_2 \end{pmatrix} + \boldsymbol{B} \begin{pmatrix} v_1 \\ v_2 \end{pmatrix} \tag{1}$$

where

$$\boldsymbol{A} = \begin{pmatrix} L_2R_1 & L_1R_2 - L_2R_1 \\ L_mR_1 & L_1R_2 + L_mR_1 + L_mR_2 \end{pmatrix} \frac{1}{L_T} \tag{2}$$

$$\boldsymbol{B} = \begin{pmatrix} L_2 & L_1 \\ L_m & L_1 + L_m \end{pmatrix} \frac{1}{L_T} \tag{3}$$

$$L_T = L_1L_2 + L_1L_m + L_2L_m \tag{4}$$

v_1 and v_2 are the transformer average voltages produced by the incremental duty ratios Δm_1 and Δm_5, measured in the primary and secondary windings, respectively; i_1, i_2, and i_m are the currents through the primary winding, secondary winding, and magnetizing inductance, respectively.

Then, considering the output system represented by i_2 and i_m, it is possible to describe the system in the form of

$$\frac{d\boldsymbol{X}}{dt} = \boldsymbol{A} \cdot \boldsymbol{X} + \boldsymbol{B} \cdot \boldsymbol{U} \tag{5}$$

$$\boldsymbol{Y} = \boldsymbol{C} \cdot \boldsymbol{X} + \boldsymbol{D} \cdot \boldsymbol{U} \tag{6}$$

where

$$\boldsymbol{X} = \begin{pmatrix} i_m \\ i_2 \end{pmatrix}, \boldsymbol{U} = \begin{pmatrix} v_1 \\ v_2 \end{pmatrix}, \mathbf{C} = \begin{pmatrix} 1 & 0 \\ 0 & 1 \end{pmatrix}, \boldsymbol{D} = \begin{pmatrix} 0 & 0 \\ 0 & 0 \end{pmatrix}. \tag{7}$$

Equations (5)–(7) represent the well-known state-space equations of the system described in [23]. Still, according to the work in [23], the system is controllable because the controllability matrix represented in (8) is full rank

$$\boldsymbol{Q} = \begin{pmatrix} \boldsymbol{B} & \boldsymbol{A} \cdot \boldsymbol{B} \end{pmatrix}. \tag{8}$$

The transfer function of the system can be obtained by applying the Laplace transform, resulting in

$$H(s) = \boldsymbol{C} \cdot (s\boldsymbol{I} - \boldsymbol{A})^{-1} \cdot \mathbf{B} + \mathbf{D} = (s\boldsymbol{I} - \boldsymbol{A})^{-1} \cdot \mathbf{B}. \tag{9}$$

The time response of the system can be obtained from the inverse transform of (9). It is also worth mentioning that all eigenvalues of matrix $\mathbf{A}$ have a negative real part. Hence, if there is no input, all dc bias currents will become null after a period.

However, it is important to design output feedback to achieve step reference tracking. This task can be accomplished by adding two states $\boldsymbol{X_a}$ as seen in

$$\frac{d\boldsymbol{X_a}}{dt} = \boldsymbol{R} - \boldsymbol{Y} = \boldsymbol{R} - \boldsymbol{C} \cdot \boldsymbol{X} \tag{10}$$

where $\boldsymbol{R}$ is the matrix with step reference for each output. The additional states incorporate an integrator of the output error. Since the system has no zero in the complex plane origin, it can achieve robust tracking after a step reference and disturbance rejection. Therefore, the augmented system is represented in

$$\begin{pmatrix} \dot{\boldsymbol{X}} \\ \dot{\boldsymbol{X}}_{\boldsymbol{a}} \end{pmatrix} = \boldsymbol{A_i} \cdot \begin{pmatrix} \boldsymbol{X} \\ \boldsymbol{X_a} \end{pmatrix} + \boldsymbol{B_i} \cdot \boldsymbol{U} \begin{pmatrix} 0_{2\times2} \\ \boldsymbol{I}_{2\times2} \end{pmatrix} \cdot \boldsymbol{R} \tag{11}$$

$$\boldsymbol{Y} = \begin{pmatrix} \boldsymbol{C} & 0_{2\times2} \end{pmatrix} \begin{pmatrix} \boldsymbol{X} \\ \boldsymbol{X_a} \end{pmatrix} \tag{12}$$

where $\mathbf{0_{2\times2}}$ is a 2×2 null matrix, $\boldsymbol{I}_{\mathbf{2\times2}}$ is a 2×2 identity matrix, as well as

$$\boldsymbol{A_i} = \begin{pmatrix} \boldsymbol{A} & 0_{2\times2} \\ -\boldsymbol{C} & 0_{2\times2} \end{pmatrix}, \boldsymbol{B_i} = \begin{pmatrix} \boldsymbol{B} \\ 0_{2\times2} \end{pmatrix}. \tag{13}$$

The system dynamics can be modified by a state feedback control since all eigenvalues of a controllable system can be arbitrarily allocated as presented in [23]. In this way, to obtain the required feedback gain to accurately allocate the new eigenvalues, one can solve the Lyapunov equation represented by

$$\boldsymbol{A_i} \cdot \boldsymbol{T} - \boldsymbol{T} \cdot \boldsymbol{F} = \boldsymbol{B_i} \cdot \boldsymbol{K_L} \tag{14}$$

where $\boldsymbol{F}$ is a matrix containing the desired eigenvalues and K_L should be chosen in such a way that $\boldsymbol{O_L}$ given in the following

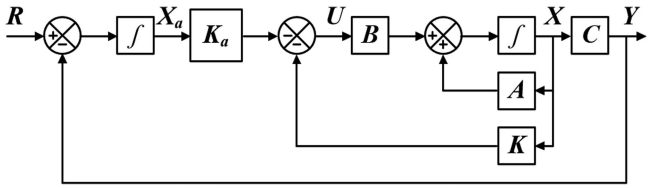

Fig. 4. Augmented system with feedback states.

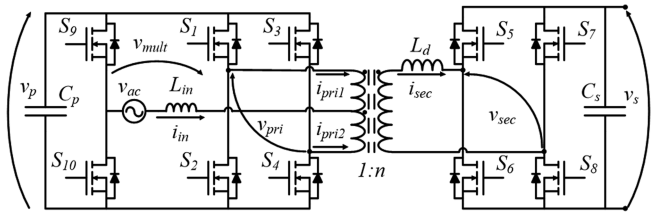

Fig. 5. Integrated single-stage AC–DC topology.

equation must be full rank and the spectral norm of matrix $\boldsymbol{K_i}$ seen in (16) is minimized:

$$\boldsymbol{O_L} = \begin{pmatrix} \boldsymbol{K_L} \\ \boldsymbol{K_L \cdot F} \end{pmatrix}. \tag{15}$$

Matrix $\boldsymbol{T}$ in (14) corresponds to the solution of the equation and can be computationally solved using a Matlab function called *Lyap*, for instance. From $\boldsymbol{T}$, one can obtain the feedback state gain using

$$\boldsymbol{K_i} = \begin{pmatrix} c\boldsymbol{K} \\ \boldsymbol{K_a} \end{pmatrix} = \boldsymbol{K_L \cdot T^{-1}} \tag{16}$$

where $\boldsymbol{K}$ and $\boldsymbol{K_a}$ are the feedback state gains of the former and augmented system, respectively.

It is worth mentioning that the new eigenvalues chosen in matrix $\boldsymbol{F}$ must be different from those of matrix $\boldsymbol{A}$. Otherwise, the resulting matrix $\boldsymbol{T}$ could be singular, and no response would be obtained in (16). A good choice for matrix F is the modal form as seen in

$$\boldsymbol{F} = \begin{pmatrix} \alpha & \beta & 0 & 0 \\ -\beta & \alpha & 0 & 0 \\ 0 & 0 & \lambda_1 & 0 \\ 0 & 0 & 0 & \lambda_2 \end{pmatrix}. \tag{17}$$

Parameters α and β are the real and imaginary parts of the complex conjugated desired eigenvalues, respectively; λ_1 and λ_2 are two additional eigenvalues incorporated into the matrix due to the augmented states. These eigenvalues must be chosen with a large negative real part to provide a much faster behavior of the controller while keeping the chosen dynamic specifications in the output. If matrix F is chosen in the modal form, a simple solution lies in using a given matrix $\boldsymbol{K_L}$ with at least one nonnull element for each diagonal block F as seen in

$$\boldsymbol{K_L} = \begin{pmatrix} 1 & 0 & 1 & 1 \\ 1 & 1 & 0 & 1 \end{pmatrix}. \tag{18}$$

Moreover, the feedback gain can also be obtained from any other optimization method. For instance, the linear quadratic regulator can be used.

This solution aims at obtaining an optimal and minimal computational burden using a quadratic expression with two cost matrixes as stated in [24].

Finally, the complete system with augmented states and feedback states can be seen in Fig. 4. The related matrixes are given in (19), whereas the output system is represented in (20)

$$\begin{pmatrix} \dot{\boldsymbol{X}} \\ \dot{\boldsymbol{X}}_{\boldsymbol{a}} \end{pmatrix} = \begin{pmatrix} \boldsymbol{A - B \cdot K} & \boldsymbol{-B \cdot} K_a \\ \boldsymbol{-C} & \boldsymbol{0}_{2\times 2} \end{pmatrix} \begin{pmatrix} \boldsymbol{X} \\ \boldsymbol{X_a} \end{pmatrix} + \begin{pmatrix} \boldsymbol{0}_{2\times 2} \\ \boldsymbol{I}_{2\times 2} \end{pmatrix} \cdot \boldsymbol{R} \tag{19}$$

$$\boldsymbol{Y} = \begin{pmatrix} \boldsymbol{C} & \boldsymbol{0}_{2\times 2} \end{pmatrix} \begin{pmatrix} \boldsymbol{X} \\ \boldsymbol{X_a} \end{pmatrix}. \tag{20}$$

It is worth mentioning that this system can be implemented in architectures, such as digital signal processors, or advanced reduced instruction set computer (RISC) machines, among others by using only two integrators and matrix multiplication. As previously mentioned, it can achieve robust step tracking and disturbance rejection while being inherently coupled for regulating both currents simultaneously.

IV. AC–DC Converter Topology and Experimental Prototype

The previously discussed control system is applied in an integrated single-stage ac–dc topology, which is shown in Fig. 5 and described in detail in [25], [26], and [27]. To better present the equivalence between the studied topology and the DAB, in this section, the ac–dc topology, main currents, and general control strategy are briefly discussed. The topology can be built with a transformer with a center tap or a two-winding transformer with coupled inductors to obtain the interleaved operation. Both structures are quite similar from a magnetic perspective. In the center-tapped structure, the input current is equally shared between both primary windings. The opposite direction of the currents in the coils cancels the magnetic field produced by this low-frequency component, as it is possible to analyze this structure using the equivalent system shown in Fig. 3. This center-tapped transformer was incorporated into the structure in [26] to reduce the size and losses as part of a three-phase solid-state transformer (SST). Preliminary results were presented for a low-power prototype as well. An extensive study of the topology was carried out in [27] to validate its applicability to medium-voltage railways. A complete loss analysis was performed, and steady-state and dynamic results were presented.

These studies performed an in-depth analysis of the topology, whereas the current work will not focus on the modulation scheme and switching states. In turn, this section is dedicated to the experimental setup and the analysis of accuracy related to the measured current bias acquisition precision and the proposed control strategy verification.

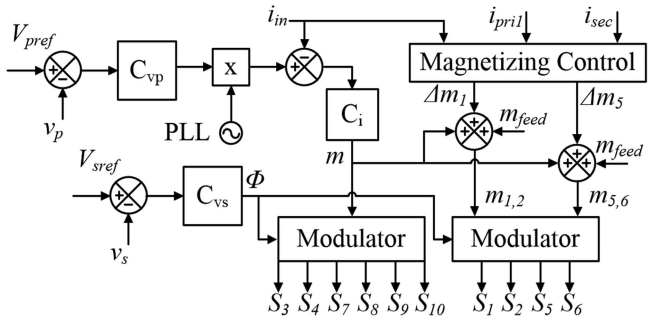

Fig. 6. Block diagram of the proposed control strategy on the selected power converter topology.

The primary-side bridge is responsible for obtaining a five-level voltage v_{mult}, as well as achieving unity input power factor and a sinusoidal input current. It also generates a three-level voltage to be applied to an isolation high-frequency transformer transferring power through the PS angle. To accomplish all these tasks, the integrated stage is composed of three legs, that is, two legs at high frequency (S_1–S_2 and S_3–S_4) and one leg at low frequency (S_9–S_{10}). It also comprises a center-tapped transformer for achieving the interleaved operation of the branches while reducing the current stresses.

Analyzing the proposed methodology applied in such topology is interesting since it uses a sinusoidal modulation technique in the primary bridge. Thus, an aggressive dc bias current control will directly impact the input current shape.

Fig. 6 shows the proposed control approach applied in the ac–dc power converter topology. Therefore, it employs a cascade control loop for power factor correction and regulation of dc-link voltage v_p. The secondary dc-link voltage v_s is regulated using PS control. The magnetizing current control relies on measuring the primary current i_{pri1} and secondary current i_{sec}. Since i_{pri1} comprises half the input current i_{in}, this latter quantity must be used to eliminate the low-frequency component. However, it is not necessary to use another sensor since i_{in} is already measured to provide power factor correction. On the other hand, a second method lies in measuring i_{pri1} and i_{pri2} in a differential manner with the same sensor to remove the low-frequency component as in [17]. Equation (21) shows how it is possible to obtain the magnetizing current for both methodologies

$$i_{\mathrm{mag}} = \frac{i_{\mathrm{pri1}} - i_{\mathrm{pri2}}}{2} - i_{\mathrm{sec}} n = \frac{i_{\mathrm{in}}}{2} + i_{\mathrm{pri1}} - i_{\mathrm{sec}} n \qquad (21)$$

where n is the transformer turns ratio.

Equation (21) considers that the experimental setup was modeled primary side referred. The magnetizing control adds a given value (Δm_1 and Δm_5) to the duty ratios of legs S_1–S_2 and S_5–S_6 while correcting properly the dc bias, as discussed in Sections II and III. A feedforward signal m_{feed} is also added to assist the control performance. This signal and its effect are better discussed in Section IV.

Table I shows the converter specifications, which comprise a single-module part of a three-phase SST rated at 75 kW [26]. Table II lists the components used in the experimental setup. All signals are applied to an analog low-pass filter tuned at 10 kHz.

TABLE I
CONVERTER SPECIFICATIONS

Parameter	Value
Primary dc-link voltage	V_p = 544 V
Secondary dc-link voltage	V_s = 650 V
RMS input voltage	V_{ac} = 308 V
Output power	P_o = 8.33 kW
Switching frequency	f_{sw} = 20 kHz
Line frequency	f_{line} = 60 Hz
Primary peak current	$Ipeak_{pri1}$ = 53.4 A
Secondary peak current	$Ipeak_{pri2}$ = 26.5 A
Input peak current	$Ipeak_{in}$ = 38 A

TABLE II
COMPONENTS USED IN THE PROTOTYPE

Device	Value	Description
Input inductor	L_{in} = 360 μH	Sendust core MMTS26T13325 N_{Lin} = 93 turns 17xAWG20
Energy transfer inductor	L_d = 93 μH	Iron dust core MMT002T7713 N_{Ld} = 94 turns 10xAWG20
Power transformer	L_m = 32 mH L_p = 8 μH L_s = 10 μH R_p = 42 mΩ R_s = 78 mΩ	Two ferrite cores MMT1398530 N_p = 52 turns 7xAWG20 N_s = 62 turns 3xAWG18
Semiconductor	MOSFET	CREE CCS050M12CM2
DsPIC and ADC	DsPIC	Microchip 33EP16GS502, 12 b ADC Reference voltage V_{ADC}=3.3 V
Current sensor	CKSR-50	Sensitivity = 12.5 mV/A Reference voltage V_{CKSR} = 5 V I_{pri1}: Gain 0.82/19.7- mA resolution I_{sec}: Gain 0.81/20.0- mA resolution I_{in}: Gain 0.63/23.4 -mA resolution

The current measurement also employs an analog gain circuit to better adequate the measuring range.

The dc bias current is obtained through the average of eight measurements equally spaced in the switching period, starting from the zero point of the PWM carrier associated with S_1. Thus, the resulting dc bias will correspond to the respective average value for any duty cycle and PS angle.

The maximum current resolution can be obtained considering the current sensor sensitivity, the analog-to-digital converter (ADC) resolution, and the maximum current peak. Besides, the currents can increase up to 20% above the rated value. Considering the transformer magnetizing inductance, the magnetizing current peak will be on the order of 239 mA with a magnetic flux density of about 346 mT at the rated operating point. For a maximum magnetic flux density of 470 mT, the magnetizing current could reach 283 mA, allowing an offset of at least 65 mA before saturation. Therefore, the measurement system is assumed to be accurate enough for the application. It is worth mentioning that the current sensor has an internal offset of 2.5 V while the ADC middle point is 1.65 V and is used as a resistive divider to adequate the signal, which reduces the precision. Hence, using a current sensor with the same reference voltage as the ADC could improve even more the current measurement resolution.

TABLE III
CONTROLLER PARAMETERS

Parameter	Value
ω_n	27.32
ξ	0.59
α	-16.15
β	22.03
λ_1=λ_2	-100
$K_i(1\times1)$	-7.217
$K_i(1\times2)$	0.783
$K_i(1\times3)$	415.955
$K_i(1\times4)$	-72.411
$K_i(2\times1)$	-7.205
$K_i(2\times2)$	0.645
$K_i(2\times3)$	408.932
$K_i(2\times4)$	-71.2511

The inductances of the transformers were obtained using the Agilent LCR meter 4263B, combined with the methodology presented in [28] and a 93-μH external inductor is added to the secondary side to improve power delivery.

Table III presents the controller parameters. A natural frequency $\omega_n = 27.32$ rad/s was chosen for the desired pole, with a damping ratio $\xi = 0.59$. Parameters α and β are the real and imaginary parts of a pair of complex conjugate poles, respectively, whereas λ_1 and λ_2 are the reals part of the additional poles. Table III also shows the feedback gain calculated from (14) and (16). The loop has a slow dynamic response so that it does not impact the harmonic content of the input current.

Fig. 7 shows the algorithm implemented. This algorithm was implemented on an FPGA Artix 7 from Xilinx using the fixed point reaching a low latency. All the calculations in the loop take only 230 ns. The FPGA was chosen for the calculations since it is possible to perform concurrent calculations for additional modules.

V. EXPERIMENTAL RESULTS

A. Experimental Results Under No-Load Condition

The magnetizing current has a small magnitude and high-power converters with high current and fast semiconductors, such as silicon carbide MOSFET produces a great amount of noise. To better visualize the magnetizing current, in this section, it will show only results under the no-load condition.

To better understand the dc bias issue, Fig. 8 shows the system under the steady-state condition with only a dc source in the primary dc link and a constant sinusoidal modulation. The secondary is not connected, and no control loops are enabled. At a lower dc-link voltage, the transformer changes the duty cycle along with the voltage line to achieve power factor correction, as shown in Fig. 8(a) in detail.

It can be seen that even under such ideal conditions, nonidealities and small differences in the system cause a low-frequency oscillation in the magnetizing current (I_{mag}). As shown in Fig. 8(b), this oscillation reaches the saturation limit at the rated dc-link voltage.

It is possible to mitigate this oscillation and obtain the result in Fig. 8(c) by adding the feedforward signal shown in Fig. 8(d).

Algorithm

Constants Definition Variables definitions

States: Imag, Isec
States with feedback gain: X1_k, X2_k
Additional States: Xa1_0k, Xa1_1k, Xa2_0k and Xa2_1k
Additional States with feedback gain: Xa1_k, Xa2_k,
Error: e1_0k, e1_1k, e2_0k, e2_1k;
Control output: u1,u2;

Current references: ImagRef, IsecRef
Sample time: Ta;
Feedback gain: Ka11, Ka12, Ka21, Ka22, Ki11, Ki12, Ki21,Ki22;
Nominal Voltage bus: Vp and Vs

Logic Loop

Loop
Step 1: Currents acquisition
Acquire Imag and Isec
Step 2: Calculate current error
e1_0k = ImagRef – Imag
e2_0k = IsecRef – Isec
Step 3: Determine the additional states by integrating the error
Xa1_0k = Xa1_1k + Ta*(e1_0k + e1_1k)/2
Xa2_0k = Xa2_1k + Ta*(e2_0k + e2_1k)/2
Step 4: Apply feedback state to all states variables
X1_k = Ki11*Imag + Ki12*Isec
X2_k = Ki21*Imag + Ki22*Isec
Xa1_k = Ka11*Xa1_0k + Ki12*Xa2_0k
Xa2_k = Ka21*Xa1_0k + Ki22*Xa2_0k
Step 5: Determine control signal
u1 = (Xa1_k - X1)/Vp
u2 = (Xa2_k - X2)/Vs
Step 6: Update signals
e1_1k = e1_0k
e2_1k = e2_0k
Xa1_1k = Xa1_1k
Xa2_1k = Xa2_0k
Step 7: Increment S1 e S5 duty cycle
End loop

Fig. 7. Algorithm implemented.

The amplitude of this signal corresponds to less than 1% of the maximum duty cycle and compensates only for low-frequency oscillation. However, any dc bias should be mitigated by the control loop.

Then, Fig. 9 presents a reference step applied to the magnetizing current, that is, from -80 to 80 mA. In this case, the secondary side is connected, and all control loops are enabled but still under the no-load condition. The magnetizing current in Fig. 9(a) reaches the steady state at approximately 50 ms but the secondary current I_{sec} and its measured value $I_{\mathrm{sec}\,M}$ in Fig. 9(b) do not change.

The acquisition system can correctly measure the currents with the secondary connection. The output control signals of both bridges have approximately the same shape but with slightly different values as evidenced in Fig. 9(c) and (d). Both magnitudes are very small, that is, below 0.5% of the switching period, thus minimizing the impact on the input current. The

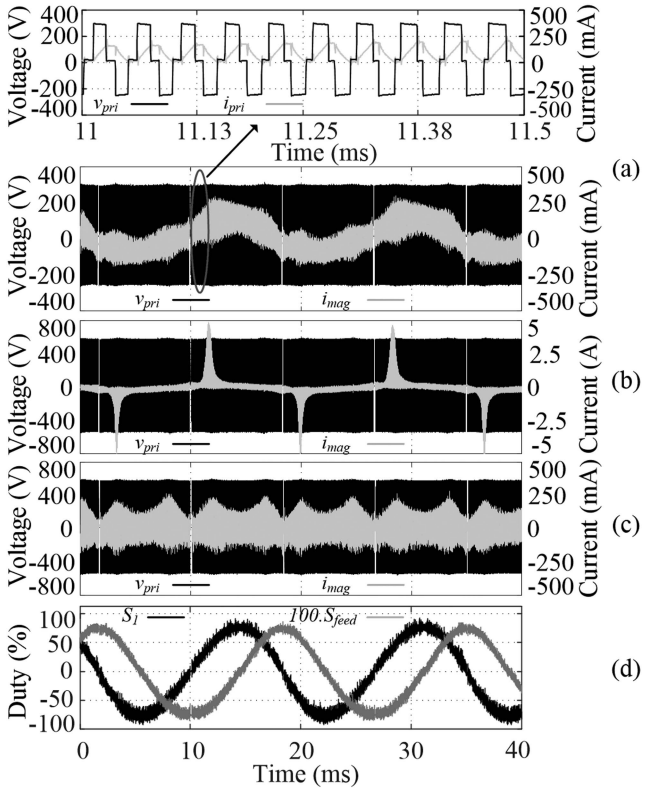

Fig. 8. Steady-state behavior. (a) Half of rated primary voltage and i_{mag}. (b) Rated primary voltage and i_{mag}. (c) Primary voltage and i_{mag} with feedforward. (d) Modulation and feedforward signals.

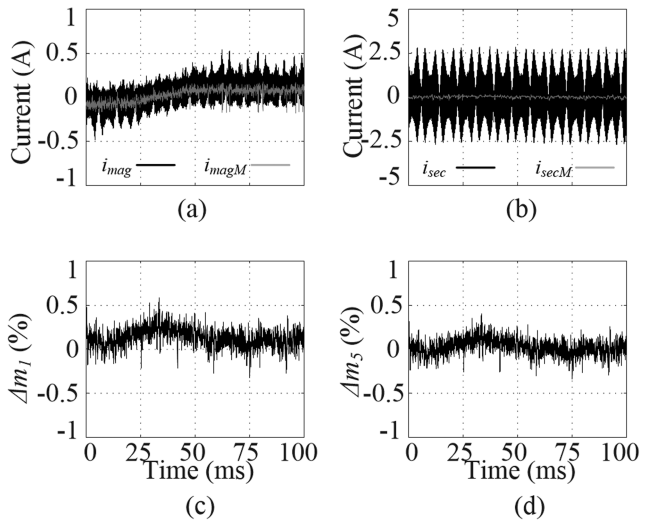

Fig. 9. Measured magnetizing current step. (a) Instantaneous and average i_{mag}. (b) Instantaneous and average i_{sec}. (c) Primary output control signal. (d) Secondary output control signal.

PWM resolution is 0.02% of the switching period, that is, 10 ns, producing a minimum magnetizing current dc bias of 209 nA when considering the adopted magnetizing inductance.

B. Experimental Results Under Load Condition

Fig. 10 represents the converter operating in a steady state under the rated power condition. Fig. 10(a) presents the primary and secondary dc-link voltages, both of which have a 120-Hz

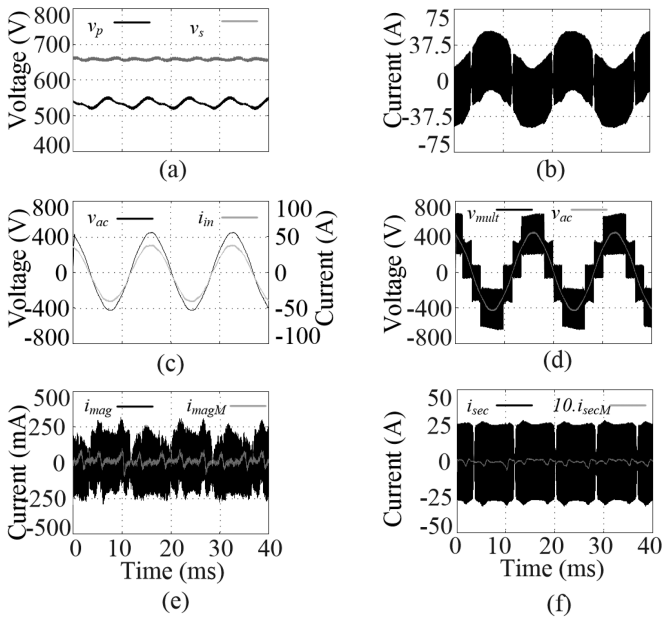

Fig. 10. Measured steady-state behavior. (a) Primary and secondary dc-link voltages. (b) Primary current. (c) Input current and input voltage. (d) Multilevel and input voltage. (e) Instantaneous and average i_{mag}. (f) Instantaneous and average i_{sec}.

component and are regulated at their respective nominal values. Fig. 10(b) shows the primary current through one winding, which has a low-frequency component due to the center-tapped structure. The power factor is nearly unity and the total harmonic distortion (THD) of the input current is 3.73% according to Fig. 10(c). Fig. 10(d) shows the voltage synthesized by the converter in phase with the input voltage. It is worth mentioning that the control loop was tuned to have little impact on the harmonic content of the current. A 10 times faster control loop was also tested, relocating the system poles to a larger negative value, and the THD increased by only 2%. However, a faster control loop causes high current spikes because the measured currents are very noisy as shown in Fig. 10(e) and (f), thus leading to transformer saturation.

Fig. 11 shows a magnetizing current step. The converter has no dc bias initially, but the magnetizing current reference suddenly changes at 20 ms to obtain a small value of 80 mA. This bias produces some small current peaks as shown in Fig. 11(a) because the transformer saturation limit is very tight, whereas an effective control approach is essential to remove any dc bias. A higher step could saturate the transformer with very high current peaks, thus enabling the current protection and turning OFF the converter. The control loop takes about 40 ms to achieve the steady state. The secondary current shown in Fig. 11(b) is not affected as well.

Fig. 11(c) and (d) show the current measured value to evidence the impact of the step reference. The magnetizing current in Fig. 11(c) presents a dc bias with small current peaks due to transformer saturation while the secondary current remains with zero average value. The measurement system can still acquire the measured value even with a highly noisy signal during the operation at the rated power. The peaks due to the transformer reaching its saturation limit produce a noise in the

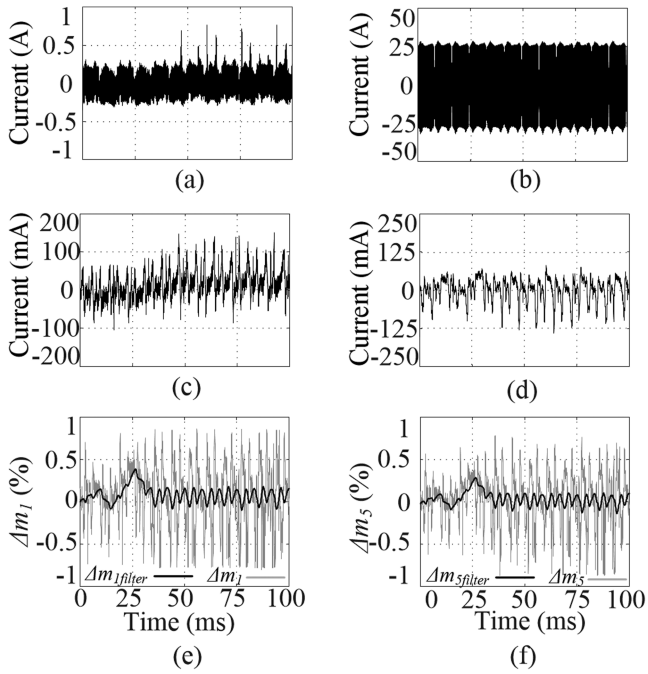

Fig. 11. Measured magnetizing current step. (a) Instantaneous I_{mag}. (b) Instantaneous i_{sec}. (c) Average i_{mag}. (d) Average i_{sec}. (e) Primary acquired and filtered output control signal. (f) Secondary acquired and filtered output control signal.

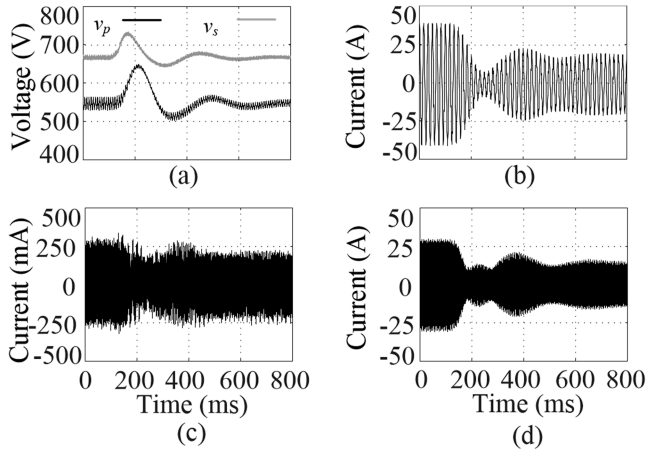

Fig. 12. Load step of 50%. (a) Primary and secondary DC-link voltages. (b) Input current. (c) Magnetizing current. (d) Secondary current.

control output as can be seen in Fig. 11(e) and (f) showing the primary and secondary output control signals, respectively. In these figures, a low-pass filter version of the signal to better visualize the dynamics was added. A situation with a small bias could be presented reducing the noise, avoiding the transformer saturation, but the effect in the offset would be difficult to see. Considering the low-pass filter in the control signal, it can be seen a profile similar to the one at no load in Fig. 9.

A load step of 50%, while the PS angle changes from 30° to 15°, is applied to the converter in Fig. 12. Fig. 12(a) shows that the dc-link voltages have an overshoot of 10%. The input current reduction can be seen in Fig. 12(b). Fig. 12(c) and (d) represent the magnetizing current and secondary current, respectively. The magnetizing does not present saturation peaks even when the PS

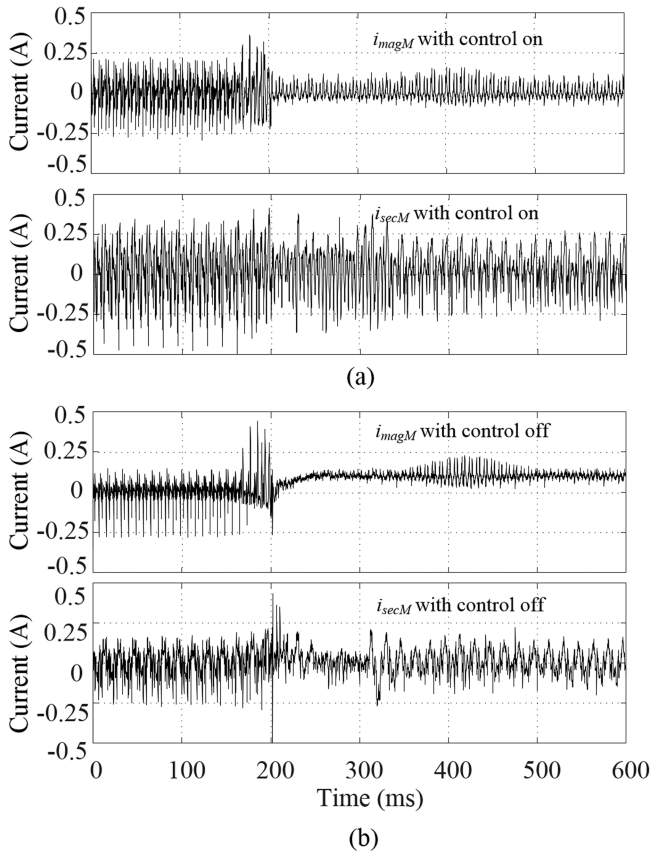

Fig. 13. Response of turning OFF the proposed control. (a) Instantaneous and average i_{mag}. (b) Average i_{mag}.

angle and dc-link voltages vary owing to the high load change together with very tight transformer saturation bounds. Both the magnetizing and secondary currents are well limited and reach the steady state with a zero-average value without enabling any protection system during the tests.

It is worth mentioning that it is difficult to start the converter operation without the proposed control system. Fig. 13 shows what happens when the control is turned OFF. Initially, the magnetizing current has zero dc offset, obtained with the proposed control. The control is turned OFF at 200 ms and the duty cycle and PS angle variations inherent in the integrated stage inevitably led to a positive dc bias, which causes transformer saturation with high current peaks, as shown in Fig. 13(a). In Fig. 13(b), it is shown the measured average magnetizing current evidencing that the magnetizing current has a small dc bias that saturates the transformer. In this condition, the current peaks can enable current protection by turning OFF the converter.

VI. Conclusion

This work has proposed a multivariable dc bias current control method applied to an integrated single-stage DAB-based converter. It has been demonstrated that the dc bias can be produced by both bridges and the control loop must act on both sides of the converter. The mathematical modeling based on state-space equations considers that the system characteristics are inherently coupled. The proposed control solution is derived using state feedback, based on the incorporation of more states

to achieve robust tracking and noise rejection. The feedback gain is obtained using the Lyapunov equation but other optimization methods could be used instead.

The control system was tested in an integrated single-stage DAB-based converter prototype rated at 8.33 kW. An offset of 23.4 mA could be measured while the transformer was designed to tolerate a minimum offset of 65 mA, showing that the acquisition system has a high enough resolution. The prototype was tested with a reference change from -80 to 80 mA under the no-load condition and from zero to 80 mA under the rated load condition, evidencing the reference tracking capability.

The output control signals are very small, that is, less than 0.5% of the switching period, causing a negligible impact on the input current THD. Even a 10 times faster control increased the THD by only 2%. The system was also tested under a load step condition showing that the control system is still capable of regulating the dc biases even during a significant change of the operating point, and its absence produced high current peaks due to magnetic saturation, which can cause the failure of the converter.

Considering all the presented results, the proposed multivariable control can achieve the mitigation of all dc bias currents even during a wide variation of duty cycle and PS angle in the assessed integrated converter. Moreover, it is possible to state that the proposed control strategy is quite suitable for high-power applications, where only dc bias mitigation by high-frequency modulation approaches is not enough. Finally, since the mathematical analysis relies on well-established equations, it can be promptly extended to any DAB-based topology.

REFERENCES

[1] P. Abraham, *Switching Power Supply Design*, 2nd ed. New York, NY, USA: McGraw-Hill, 1997.

[2] L. Shu, W. Chen, Z. Lin, D. Ma, X. He, and W. A. Syed, "DC bias study for DC-DC dual-active-bridge converter," in *Proc. IEEE 4th Southern Power Electron. Conf.*, 2018, pp. 1–5.

[3] M. Wattenberg, U. Schwalbe, and M. Pfost, "Impact of DC-bias on dual active bridge control and how to avoid it," in *Proc. 21st Eur. Conf. Power Electron. Appl.*, 2019, pp. P.1–P.8.

[4] "Phase-shifted full bridge DC/DC power converter design guide," Application Note - TIDU248T, Texas Instruments Incorporated, Dallas, TX, USA, May 2014.

[5] "UCC28950/UCC28951 600-W, Phase-shifted full bridge," Application Note – SLUA560D, Texas Instruments Incorporated, Dallas, TX, USA, Jun. 2011.

[6] R. W. A. A. De Doncker, D. M. Divan, and M. H. Kheraluwala, "A three-phase soft-switched high-power-density DC/DC converter for high-power applications," *IEEE Trans. Ind. Appl.*, vol. 27, no. 1, pp. 63–73, Jan./Feb. 1991.

[7] Q. Bu, H. Wen, H. Shi, and Y. Zhu, "A comparative review of high-frequency transient DC bias current mitigation strategies in dual active bridge DC–DC converters under phase-shift modulations," *IEEE Trans. Ind. Appl.*, vol. 58, no. 2, pp. 2166–2182, Mar./Apr. 2022.

[8] B. Zhao, Q. Song, W. Liu, and Y. Zhao, "Transient DC bias and current impact effects of high-frequency-isolated bidirectional DC–DC converter in practice," *IEEE Trans. Power Electron.*, vol. 31, no. 4, pp. 3203–3216, Apr. 2016.

[9] S. Zhou, C. Sun, S. Hu, G. Chen, and X. Li, "Improved load transient response of a dual-active-bridge converter," in *Proc. Int. Power Electron. Conf.*, 2018, pp. 370–374.

[10] T. Dai et al., "Research on transient DC bias analysis and suppression in EPS DAB DC-DC converter," *IEEE Access*, vol. 8, pp. 61421–61432, 2020.

[11] Q. Bu, H. Wen, J. Wen, Y. Hu, and Y. Du, "Transient DC bias elimination of dual-active-bridge DC–DC converter with improved triple-phase-shift control," *IEEE Trans. Ind. Electron.*, vol. 67, no. 10, pp. 8587–8598, Oct. 2020.

[12] J. Voss, S. P. Engel, and R. W. De Doncker, "Control method for avoiding transformer saturation in high-power three-phase dual-active bridge DC–DC converters," *IEEE Trans. Power Electron.*, vol. 35, no. 4, pp. 4332–4341, Apr. 2020.

[13] B. R. de Almeida, J. W. M. de Araújo, P. P. Praça, and D. de S. Oliveira, "A single-stage three-phase bidirectional AC/DC converter with high-frequency isolation and PFC," *IEEE Trans. Power Electron.*, vol. 33, no. 10, pp. 8298–8307, Oct. 2018.

[14] S. Dutta and S. Bhattacharya, "A method to measure the DC bias in high frequency isolation transformer of the dual active bridge DC to DC converter and its removal using current injection and PWM switching," in *Proc. IEEE Energy Convers. Congr. Expo.*, 2014, pp. 1134–1139.

[15] L. Zhu, H. Bai, A. Brown, and M. McAmmond, "Design a 400 V–12 V 6 kW bidirectional auxiliary power module for electric or autonomous vehicles with fast precharge dynamics and zero DC-bias current," *IEEE Trans. Power Electron.*, vol. 36, no. 5, pp. 5323–5335, May 2021.

[16] Z. Gao et al., "A transformer flux balancing scheme based on magnetizing current harmonic in dual-active-bridge converters," in *Proc. IEEE Appl. Power Electron. Conf. Expo.*, 2021, pp. 1894–1899.

[17] P. Yao, X. Jiang, P. Xue, S. Ji, and F. Wang, "Flux balancing control of ungapped nanocrystalline core-based transformer in dual active bridge converters," *IEEE Trans. Power Electron.*, vol. 35, no. 11, pp. 11463–11474, Nov. 2020.

[18] K. Sakuma, K. Shigeuchi, J. Xu, N. Shimosato, and Y. Sato, "Decoupling control method for eliminating DC bias flux of high frequency transformer in a bidirectional isolated AC/DC converter," in *Proc. Int. Power Electron. Conf.*, 2018, pp. 3522–3527.

[19] A. Gertsman and S. Ben-Yaakov, "Zeroing transformer's DC current in resonant converters with no series capacitors," in *Proc. IEEE Energy Convers. Congr. Expo.*, 2010, pp. 4028–4034.

[20] F. P. Dawson, "DC-DC converter interphase transformer design considerations: Volt-seconds balancing," *IEEE Trans. Magn.*, vol. 26, no. 5, pp. 2250–2252, Sep. 1990.

[21] G. Ortiz, L. Fässler, J. W. Kolar, and O. Apeldoorn, "Flux balancing of isolation transformers and application of 'the magnetic ear' for closed-loop volt–second compensation," *IEEE Trans. Power Electron.*, vol. 29, no. 8, pp. 4078–4090, Aug. 2014.

[22] R. Prochazka, J. Hlavacek, and K. Draxler, "Magnetic circuit of a high-voltage transformer up to 10 kHz," *IEEE Trans. Magn.*, vol. 51, no. 1, Jan. 2015, Art. no. 2800204.

[23] C. T. Chen, *Linear System Theory and Design*, 3rd ed. London, U.K.: Oxford Univ. Press, 1999.

[24] D. O. Neacşu and A. Sîrbu, "Design of a LQR-based boost converter controller for energy savings," *IEEE Trans. Ind. Electron.*, vol. 67, no. 7, pp. 5379–5388, Jul. 2020.

[25] D. D. A. Honório, D. S. Oliveira, L. H. S. C. Barreto, and F. L. M. Antunes, "A solid state transformer based on a single-stage AC-DC modular cascaded multilevel converter," in *Proc. 18th Eur. Conf. Power Electron. Appl.*, 2016, pp. 1–9.

[26] J. W. M. Araújo, D. S. O. Júnior, P. P. Praça, L. H. S. C. Barreto, D. de A. Honório, and F. L. M. Antunes, "Experimental validation of a basic module based on a single-stage AC-DC converter, feasible to solid-state transformer applications," in *Proc. 21st Eur. Conf. Power Electron. Appl.*, 2019, pp. P.1–P.7.

[27] D. D. A. Honório, J. W. M. de Araújo, L. H. S. C. Barreto, and D. D. S. Oliveira, "Three-leg integrated stage AC–DC solid-state transformer feasible for MV railway applications," *IEEE J. Emerg. Sel. Topics Power Electron.*, vol. 10, no. 4, pp. 3711–3720, Aug. 2022.

[28] M. K. Kazimierczuk, *High-Frequency Magnetic Components*, 2nd ed. Hoboken, NJ, USA: Wiley, 2014.

José W. M. de Araújo was born in Fortaleza, Brazil, in 1988. He received the Ph.D. degree in electrical engineering from the Federal University of Ceará, Fortaleza, in 2022.

He is currently a Researcher with the Group of Power Processing and Control (GPEC), Federal University of Ceará, working on vehicle chargers. His research interests include static power converters, soft commutation, and renewable energy applications.

Dalton de A. Honório (Member, IEEE) received the bachelor's, master's, and Doctoral degrees in electrical engineering from the Federal University of Ceará, Fortaleza, Brazil, in 2010, 2013, and 2018, respectively.

In 2015, he was with Oak Ridge National Laboratory (ORNL), Oak Ridge, TN, USA, due to a 6-month staysandwich Ph.D. period. He is currently an Adjunct Professor with the Federal University of Ceará, where he participates in research focused on power conditioners, being the Head of the Power Conditioners Laboratory (LCE) and a Member of the Power Processing and Control Group (GPEC), developing extension and research projects aligned with industry companies. His current research interests include power electronics applications, specifically on high conversion ratio dc–dc converters, as well as cascaded multilevel converters and modular multilevel converters applied in solid-state transformers, and his early work in these fields mainly revolved around the following topics: proposing new topologies, modulation technique analysis, control techniques for multilevel structures, and control schemes for ac machine drives.

Dr. Honório has been a member of the Brazilian Power Electronics Society (SOBRAEP) since 2011, and he was its first Secretary during the biennium 2022.2023. He has also been a member of the IEEE Power Electronics Society (PELS) since 2016, located in the Northeast Brazil Section, R-9.

Demercil de S. Oliveira Jr. (Senior Member, IEEE) received the B.Sc. and M.Sc. degrees in electrical engineering from the Federal University of Uberlândia, Uberlândia, Brazil, in 1999 and 2001, respectively, and the Ph.D. degree in electrical engineering from the Federal University of Santa Catarina, Florianópolis, Brazil, in 2004.

He has been a Professor with the Federal University of Ceará, Fortaleza, Brazil, since 2005. His research interests include power converter topologies, soft-switching techniques, three-phase dc–dc power conversion, solid-state transformers, and renewable energy applications.